OPTOELECTRONICS AND ADVANCED MATERIALS – RAPID COMMUNICATIONS Vol. 4, No. 4, April 2010, p. 480 - 497

Analytical modeling and ATLAS simulation of N^+-$Hg_{0.69}Cd_{0.31}Te$ /n^0- $Hg_{0.78}Cd_{0.22}Te$/$p^+Hg_{0.78}Cd_{0.22}Te$ *p*-i-*n* photodetector for long wavelength free space optical communication

A. D. D. DWIVEDI, P. CHAKRABARTI*
Centre for Research in Microelectronics, Department of Electronics Engineering
Institute of Technology, Banaras Hindu University, Varanasi-221005 India

In this paper we report an analytical modeling of N^+-$Hg_{0.69}Cd_{0.31}Te$ /n^0 $Hg_{0.78}Cd_{0.22}Te$ /p^+-$Hg_{0.78}Cd_{0.22}Te$ *p*-i-*n* photodetector for long wavelength free space optical communication. The results obtained on the basis of our model have been compared and contrasted with the simulated results using ATLAS™. The photodetector has been studied in respect of energy band diagram, electric field profile, doping profile, dark current, resistance area-product, quantum efficiency, spectral response, responsivity and detectivity by analytical method using closed form equations and also been simulated by using device simulation software ATLAS™ from SILVACO® international. The photodetector exhibits a high value of quantum efficiency ~80 %, responsivity ~7 A/W, specific detectivity ~3.44×10^{11} $mHz^{1/2}W^{-1}$at wavelength10.6µm, dark current of the order of 10^{-11} A. The estimated noise equivalent power (NEP) is the order of 3×10^{-18} W.

(Received September 21, 2009; accepted April 11, 2010)

Keywords: ATLAS simulation, p-i-n photodetector, Optical communication, Hg-Cd-Te

1. Introduction

Free space optical communication (FSO) is an optical communication system uses light propagating in free space to transmit data between two points. The technology is useful where the line of sight path is available between source and destination or where constrained by high costs or other facts. Therefore free space optical communication offers several advantages over conventional optical communication and radio frequency (RF) communications such as high bandwidth, low cost, ease of implementation, license free spectrum and freedom from interference. Successful implementation of free space optical communication largely depends on the availability of suitable atmospheric attenuation window for terrestrial applications and development of suitable sources and detectors for design of optical transmitters and receivers. For terrestrial applications, two strategic atmospheric attenuation windows e.g., 9.6 µm and 10.6 µm have been chosen for development of free space optical links in the long wavelength region. HgCdTe can be used to develop detectors for operation at these wavelength regions. The mole fraction of cadmium in HgCdTe can be adjusted suitably to tailor the energy bandgap of the material so as to match with the wavelengths corresponding to the above atmospheric windows [1]. We propose an N^+-$Hg_{0.69}Cd_{0.31}Te$ /n^0 $Hg_{0.78}Cd_{0.22}Te$ /p^+-$Hg_{0.78}Cd_{0.22}Te$ *p*-i-*n* photodetector for which analytical simulation by using closed form expressions has been performed and results of the same have been compared and contrasted by simulation results of ATLAS™ from SILVACO® international. N^+-$Hg_{0.69}Cd_{0.31}Te$ and n^0 $Hg_{0.78}Cd_{0.22}Te$ form heterojunction and n^0 $Hg_{0.78}Cd_{0.22}Te$ and p^+-$Hg_{0.78}Cd_{0.22}Te$ form active homojunction. In this paper we report analytical and ATLAS™ simulation results of the proposed N^+-$Hg_{0.69}Cd_{0.31}Te$ /n^0 $Hg_{0.78}Cd_{0.22}Te$ /p^+-$Hg_{0.78}Cd_{0.22}Te$ *p*-i-*n* photodetector for free space optical communication at 10.6µm atmospheric window. The device has been simulated for its electrical and optical characteristics. For electrical characterization we simulated the device in respect of its energy band diagram, electric field profile doping profile, dark current and resistance area product and for optical characterization we have studied the spectral response, quantum efficiency, responsivity and detectivity. For this purpose a closed form expression for diffusion current in dark and illuminated condition and for quantum efficiency have been derived by solving diffusion equation using appropriate boundary conditions. Results obtained from closed form expressions have been compared and contrasted from those obtained from ATLAS™ simulation.

2. Material model

Numerical computations have been carried out for theoretical characterization of N^+-$Hg_{0.69}Cd_{0.31}Te$ /n^0 $Hg_{0.78}Cd_{0.22}Te$ /p^+-$Hg_{0.78}Cd_{0.22}Te$ *p*-i-*n* photodetector for operation at temperature 77 K. The mole fraction of cadmium in the ternary MCT material has been calculated so that the bandgap energy of the material corresponds to the long wavelength cut-off value of 10.6 μm for LWIR free space optical communication. The band gap of $Hg_{1-x}Cd_xTe$ as a function of temperature, T and alloy composition, x is included in the simulation model using the following empirical formula [2]

$$E_g = -0.302 + 1.93x - 0.810x^2 + 0.832x^3 + 5.35\times10^{-4}(1-2x)\left(\frac{-1822+T^3}{255.2+T^2}\right) \quad (1)$$

The intrinsic carrier concentration was calculated using the following expression [3]

$$n_i = \left(5.24256 - 3.57290x - 4.74019\times10^{-4}T + 1.25942\times10^{-2}xT - 5.77046x^2 - 4.24123\times10^{-6}T^2\right)$$

$$\times 10^{14} E_g^{\ 3/4} T^{3/2} \exp\left(\frac{-E_g}{2kT}\right) \quad (2)$$

where k is Boltzmann 's constant. From Kane band model the hole effective mass is taken as m_h^*=0.55 m_0 and electron effective mass has been computed following [4] as

$$\frac{m_0}{m_n^*} = 1 + 2F + \frac{E_p}{3}\left(\frac{2}{E_g} + \frac{1}{E_g + \Delta}\right) \quad (3)$$

where E_p =19 eV, F=-0.8 and Δ=1.0 eV. The electron mobility has been computed using the empirical formula given by [2]

$$\mu_n = \frac{9\times10^4 s}{T^{2r}} \quad m^2/vs \quad (4)$$

where $r = (0.2x)^{0.6}$ and $s = (0.2/x)^{7.5}$ which are valid in composition range $0.2 \leq x \leq 0.6$ and temperature range T >50K.

The hole mobility has been assumed to be of the form [2]

$$\mu_n = \mu_0\left[1 + \left(\frac{p}{1.8\times10^{23}}\right)^2\right]^{-1/4} \quad (5)$$

where μ_0= 0.044 m^2/Vs

The absorption coefficient of $Hg_{1-x}Cd_xTe$ for optical carrier generation can be calculated within the Kane model, including the Moss-Burstein shift .For photon energy E< E_g (tail region), $\alpha < \alpha_g$, the absorption coefficient obeys the rule [5-6]

$$\alpha = \alpha_0 \exp\left(\frac{\delta(E - E_0)}{kT}\right) \quad (6)$$

And for photon energy E> E_g (Kane region), the absorption coefficient obeys the rule [8]

$$\alpha = \alpha_g \exp\left(\beta\left(E - E_g\right)\right)^{1/2} \quad (7)$$

where α_0 is the fitting parameter and

$$E_0 = -0.355 + 1.77x$$

$$\frac{\delta}{kT} = \frac{\ln\alpha_g - \ln\alpha_0}{E_g - E_0}$$

$$\alpha_g = -65 + 1.88T + (8694 - 10.315T)x$$

$$\beta = -1 + 0.083 + (21 - 0.13T)x$$

The expressions of the high frequency dielectric constant ε_∞ and static dielectric constant ε_s are obtained as a function of x as [2]

$$\varepsilon_\infty = 15.2 - 15.6x + 8.2x^2 \quad (8)$$

$$\varepsilon_s = 20.5 - 15.6x + 5.7x^2 \quad (9)$$

3. Carrier lifetime modeling

In order to compute the drift and diffusion components of dark current accurately, we have modeled the life time of minority carriers by considering all possible recombination mechanisms. The recombination lifetime of the carriers has been computed by taking into account the fundamental recombination mechanism (band-to-band and Auger recombination) and non fundamental recombination mechanism (Shockley-Read-Hall recombination mechanism). The radiative process takes place when free electron and hole recombine, emitting the excess energy in the form of a photon. The recombination rate for bands with spherical symmetry depends on the absorption coefficient through the equation [2]

$$G_R = \frac{8\pi}{h^3c^3}\int_0^\infty \frac{\varepsilon(E)\alpha(E)E^2 dE}{\exp(E/kT) - 1} \quad (10)$$

where $\alpha(E)$ is the optical absorption coefficient, $\varepsilon(E)$ is relative dielectric constant, h is Planck's constant and c is speed of light. Ignoring the dispersion in dielectric constant and using the high frequency value of dielectric constant the radiative lifetime can be obtained as [2]

$$\tau_R = \frac{n_i^2}{G_R(n_0 + p_0)} \quad (11)$$

where n_i is intrinsic carrier concentration, n_0 and p_0 are the thermal equilibrium concentrations for electrons and holes respectively. The dependence of α on E as analyzed by Bardeen et al can be expressed as [7]

$$\alpha(E)=\frac{2^{2/3}m_0q^2}{3\varepsilon_\infty^{1/2}\hbar^2}\left(\frac{m_n^*m_h^*}{m_0(m_n^*+m_h^*)}\right)^{3/2}\left(1+\frac{m_0}{m_n^*}+\frac{m_0}{m_h^*}\right)\left(\frac{E-E_g}{m_0c^2}\right)^{1/2} \quad (12)$$

where E_g is material band gap, m_0 is free electron mass, m_n^* is the effective mass of electrons, m_h^* is the effective mass of holes, ε_∞ is high frequency dielectric constant, E_g is material bandgap in eV and $\hbar = h/2\pi$, h being the Planck's constant. Based on this expression and assuming $E_g >$ kT and neglecting the dispersion in the dielectric we can obtain G_R as [2]

$$G_R = 5.8\times10^{-13} n_i^2 \varepsilon_\infty^{1/2}\left(1+\frac{m_0}{m_n^*}\right)\left(\frac{m_0}{m_n^*+m_h^*}\right)^{3/2} \times\left(\frac{300}{T}\right)^{3/2}\left(E_g^2+3kTE_g+3.75k^2T^2\right) \quad (13)$$

where k is Boltzmann constant, T is temperature and n_i is the intrinsic carrier concentration. Shockley-Read Hall mechanism is not an intrinsic process, as it occurs via levels in the forbidden energy gap. It may be reduced by lowering concentrations of native defects and foreign impurities. In the Shockley-Read mechanism, generation and recombination occurs via energy levels introduced by impurities or lattice defects into the forbidden energy gap.

The lifetime of carriers due to Schockley-Read-Hall recombination can be modeled in terms of trap density and capture cross-section as [8]

$$\tau_{SRH} = \frac{1}{\sigma N_f v_{th}} \quad (14)$$

where N_f is the SRH trap density, σ is the capture cross-section of minority carriers and v_{th} is the thermal velocity of the minority carriers in the active region, given by $v_{th}=\sqrt{\frac{3kT}{m_h^*}}$, for holes in n^0 region and $v_{th}=\sqrt{\frac{3kT}{m_n^*}}$ for electrons in p^+ region

The band to band Auger effects are classified in several processes according to related bands. Beattie has determined ten types of photon-less Auger recombination mechanisms that are possible in a semiconductor with a single conduction band and heavy and light hole valence bands [2]. They have the smallest threshold ($E_T \approx E_g$) and the largest combined density of states. The CHCC recombination mechanism (Auger-1) involves two electrons and a heavy hole and is dominant in n type material. The CHLH process (Auger-7) is dominant in p-type material if the spin split-off band can be ignored. For materials such as $Hg_{1-x}Cd_xTe$ where the spin split-off energy Δ is much larger than the band gap energy E_g, the probability of the Auger transition through the conduction band/heavy-hole band/spin split-off band mechanism (called CHSH or Auger S) may be negligibly small in comparison with that of the CHLH Auger transition. Hence for narrow gap $Hg_{1-x}Cd_xTe$ only Auger-1 and Auger-7 need to be considered. The Auger lifetime (τ_{Aug}) is expressed as

$$\frac{1}{\tau_{Aug}} = \frac{1}{\tau_{A1}} + \frac{1}{\tau_{A7}} \quad (15)$$

where, τ_{A1} and τ_{A7} are lifetimes of carrier due to Auger-1 and Auger-7 transitions respectively [4].The net carrier lifetime when effect of surface recombination is not taken into account is given as

$$\frac{1}{\tau} = \frac{1}{\tau_{SRH}} + \frac{1}{\tau_R} + \frac{1}{\tau_{Aug}} \quad (16)$$

4. The proposed structure

The proposed device structure is shown in Fig. 1. It consists of highly doped p^+-$Hg_{0.78}$ $Cd_{0.22}Te$ over lightly doped n^0-$Hg_{0.78}$ $Cd_{0.22}Te$ which is virtually grown on highly doped N^+-$Hg_{0.69}$ $Cd_{0.31}Te$ on a suitable substrate such as CdZnTe or sapphire using ATHENA tool of ATLAS™, device simulation software from SILVACO® international.

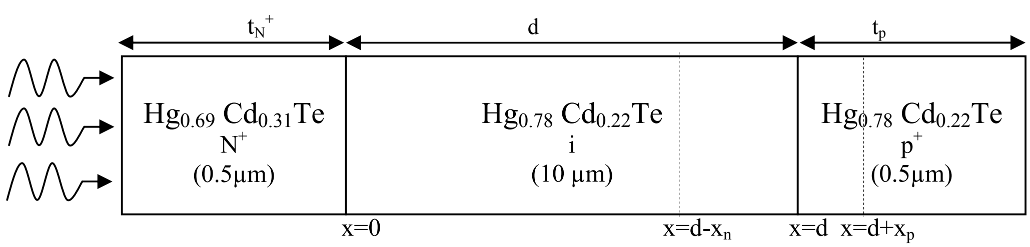

Fig. 1. Schematic structure of the proposed N^+-$Hg_{0.69}$ $Cd_{0.31}Te$ /n^0 $Hg_{0.78}$ $Cd_{0.22}Te$ /p^+-$Hg_{0.78}$ $Cd_{0.22}Te$ p-i-n photodetector.

The N^+-$Hg_{0.69}$ $Cd_{0.31}Te$ acts as window and incident light is absorbed in n^0-$Hg_{0.78}$ $Cd_{0.22}Te$ and p^+-$Hg_{0.78}$ $Cd_{0.22}Te$ regions. The operation performance of the HgCdTe based p-i-n photodetector has been studied using a two dimensional, drift–diffusion approach utilizing a commercial numerical device simulator ATLAS^{TM}. The HgCdTe based p-i-n photodiode for long wavelength free space optical communications has been proposed. The numerical simulation of *p*-i-*n* photodetector has been carried out for non degenerate semiconductor and parabolic shape of conduction band. The simulation involves solution of five decoupled equations using Newton's iteration technique. The doping of the regions has been taken analytically uniform for all regions in the above simulation. In calculation of mobility the concentration dependent ANALYTIC model has been considered. For the simulation of dark current, associated with p-i-n photodetector, AUGER, SRH and OPTICAL (band-to-band) models have been taken into account for recombination mechanisms modeling. Band-to-band standard tunneling model has been considered for tunneling mechanism. The surface recombination process at the contacts and heterointerface has been taken into account in simulation and also in analytical model. The quality of the interface has been characterized in terms of surface recombination velocity. We have taken into account the Fermi-Dirac statistics for parabolic shape of conduction band in all the calculations of carrier and doping densities. For the simulation of dark current associated with *p*-i-*n* photodetector, the optical, SRH, Augur and surface recombination rates are given as

$$R_{np}^{OPT} = C_c^{OPT}\left(pn - n_i^2\right) \tag{17}$$

$$R_{SRH} = \frac{pn - n_i^2}{\left[\tau_{p0}\left\{n + n_i \exp\left(E_t / kT\right)\right\} + \tau_{n0}\left\{p + n_i \exp\left(-E_t / kT\right)\right\}\right]} \tag{18}$$

$$R_{Aug} = C_n\left(pn^2 - nn_i^2\right) + C_p\left(p^2 n - pn_i^2\right) \tag{19}$$

$$R_{Surf} = \frac{pn - n_i^2}{\left[\tau_p^{eff}\left\{n + n_i \exp\left(E_t / kT\right)\right\} + \tau_n^{eff}\left\{p + n_i \exp\left(-E_t / kT\right)\right\}\right]} \tag{20}$$

Here C_c^{OPT} is the capture rate of carriers and $C_n \,\&\, C_p$ are and Auger coefficients for electrons and holes respectively. Here n and p are equilibrium electron and hole concentration, E_t is energy level of trap, n_i is intrinsic carrier concentration, τ_{p0} and τ_{n0} are SRH lifetime of holes and electrons respectively and τ_p^{eff} and τ_n^{eff} are effective life times of hole and electrons respectively.

5. Dark current modeling

The dark current of the p-i-n photodetector has been modeled here by considering (i) the diffusion of thermally generated carriers from neutral regions, I_{DIFF} (ii) generation-recombination of carriers in the depletion region, I_{GR} and (iii) tunneling of carriers through barriers, I_{TUN}. In order to generalize the analysis, we have however considered both trap assisted tunneling (TAT) as well as band-to-band tunneling (BTB). The tunneling component of current thus constitutes two components e.g., I_{TAT} arising from the trap assisted tunneling and I_{BTB} arising out of band-to-band tunneling. The net current can be written as

$$I = I_{DIF} + I_{GR} + I_{TAT} + I_{BTB} \tag{21}$$

Ohmic component of current and contribution due to avalanche multiplication are ignored in the present model. The relevant expressions for calculating the dark currents and the associated dynamic impedance contribution due to each of these mechanisms are outlined in the following section.

5.1 Diffusion current

For computation of diffusion component of dark current we solved continuity equation in n^0-$Hg_{0.78}$ $Cd_{0.22}Te$ region for holes and in p^+-$Hg_{0.78}$ $Cd_{0.22}Te$ region for electrons using appropriate boundary conditions. In the present structure the diffusion component of current would be dominated by the holes injected from p^+ region but we have also considered diffusion current component due to electrons injected from intrinsic n^0 region for more accurate modeling. Diffusion current density due to holes injected from p^+ region in n^0-$Hg_{0.78}$ $Cd_{0.22}Te$ region is modeled as

$$\left(J_p\right)_n = \frac{qn_i^2}{N_D}\sqrt{\frac{\mu_h kT}{q\tau_h}}\left(\frac{\gamma_p \cosh\frac{(d - x_n)}{L_p} - \sinh\frac{(d - x_n)}{L_p}}{\cosh\frac{(d - x_n)}{L_p} - \gamma_p \sinh\frac{(d - x_n)}{L_p}}\right)\left(\exp\left(\frac{qV}{kT}\right) - 1\right) \tag{22}$$

where, q is electronic charge, k is Boltzmann constant, T is the temperature, V is applied voltage, n_i is intrinsic concentration of n^0-$Hg_{0.78}$ $Cd_{0.22}Te$, N_D is donor concentration in n^0-$Hg_{0.78}$ $Cd_{0.22}Te$ region, $\gamma_p = \dfrac{S_p L_p}{D_p}$ is ratio of surface to bulk recombination velocity in n^0 region, S_p is surface recombination velocity of hole at N^+-$Hg_{0.69}$ $Cd_{0.31}Te$ and n^0-$Hg_{0.78}$ $Cd_{0.22}Te$ interface, L_p is diffusion length, D_p is diffusion coefficient, μ_h is mobility and τ_h is lifetime of holes in n^0-$In_{0.53}Ga_{0.47}As$ region. Here d is the thickness of n^0-$Hg_{0.78}$ $Cd_{0.22}Te$ region and x_n is width of depletion region in n^0 side. Diffusion current density due to electrons injected from intrinsic n^0 region in p^+-$Hg_{0.78}$ $Cd_{0.22}Te$ region is modeled as

$$(J_n)_p = \frac{qn_i^2}{N_A}\sqrt{\frac{\mu_n kT}{q\tau_n}}\left(\frac{\gamma_n \cosh\frac{(t_p - x_p)}{L_n} - \sinh\frac{(t_p - x_p)}{L_n}}{\cosh\frac{(t_p - x_p)}{L_n} - \gamma_n \sinh\frac{(t_p - x_p)}{L_n}}\right)\left(\exp\left(\frac{qV}{kT}\right) - 1\right) \quad (23)$$

where, $\gamma_n = \dfrac{S_n L_n}{D_n}$ is ratio of surface to bulk recombination velocity in p^+ region, S_n is surface recombination velocity of electrons at metal contact, L_n is diffusion length, D_n is diffusion coefficient, μ_n is mobility, N_A is acceptor concentration and τ_n is lifetime of electrons in p^+-$Hg_{0.78}$ $Cd_{0.22}Te$ region. Here x_p is the width of depletion region in p^+ side and t_p is the thickness of p^+ region. The total diffusion component of current is given as

$$J_{DIFF} = (J_p)_n + (J_n)_p \quad (24)$$

There is no any contribution in diffusion current component from N^+-$Hg_{0.69}$ $Cd_{0.31}Te$ side. The product of dynamic resistance and area (RA) is given by the reciprocal of the derivative of the current density with respect to the voltage. The diffusion component of RA product can be obtained as

$$\frac{1}{(RA)_{DIFF}} = \frac{dJ_{DIFF}}{dV}$$
$$= \left[\frac{q^2 n_i^2}{kT N_D}\sqrt{\frac{\mu_h kT}{q\tau_h}}\left(\frac{\gamma_p \cosh\frac{(d - x_n)}{L_p} - \sinh\frac{(d - x_n)}{L_p}}{\cosh\frac{(d - x_n)}{L_p} - \gamma_p \sinh\frac{(d - x_n)}{L_p}}\right) + \frac{q^2 n_i^2}{kT N_A}\sqrt{\frac{\mu_n kT}{q\tau_n}}\left(\frac{\gamma_n \cosh\frac{(t_p - x_p)}{L_n} - \sinh\frac{(t_p - x_p)}{L_n}}{\cosh\frac{(t_p - x_p)}{L_n} - \gamma_n \sinh\frac{(t_p - x_p)}{L_n}}\right)\right]\exp\left(\frac{qV}{kT}\right) \quad (25)$$

5.2 Generation recombination current

Generation recombination (GR) component of current is due to defects within the depletion region which acts as intermediate states for the thermal generation and recombination of carriers. These intermediate states are referred to as Schockley Read centers. The generation-recombination component of current density can be approximated as [9-11]

$$J_{GR} = \frac{qn_i WV}{(V_{bi} - V)\tau_{SRH}} \quad \text{for } V<0 \quad (26\text{ a})$$

$$J_{GR} = \frac{2n_i WkT}{(V_{bi} - V)\tau_{SRH}}\sinh\left(\frac{qV}{kT}\right) \quad \text{for } V>0 \quad (26\text{ b})$$

where V_{bi} is the built-in potential, V is the applied voltage, W is the width of depletion region which is function of the applied voltage and τ_{SRH} is the SRH generation recombination lifetime. The associated resistance area product in the above two cases can be approximated as

$$\left.\frac{1}{(RA)_{GR}}\right|_{V<0} = \left.\left(\frac{dJ_{GR}}{dV}\right)\right|_{V<0}$$
$$= \frac{qn_i}{\tau_{SRH}}\left(\frac{2\varepsilon_s(N_A + N_D)}{qN_A N_D}\right)^{1/2}\left(\frac{1}{(V_{bi} - V)} + \frac{V}{2(V_{bi} - V)^{3/2}}\right) \quad (27\text{ a})$$

$$\left.\frac{1}{(RA)_{GR}}\right|_{V>0} = \left.\left(\frac{dJ_{GR}}{dV}\right)\right|_{V>0}$$
$$= \frac{qn_i}{\tau_{SRH}}\left(\frac{2\varepsilon_s(N_A + N_D)}{qN_A N_D}\right)^{1/2}\left(\frac{kT}{q(V_{bi} - V)^{3/2}}\sinh\left(\frac{qV}{kT}\right) + \frac{1}{(V_{bi} - V)^{1/2}}\cosh\left(\frac{qV}{kT}\right)\right) \quad (27\text{ b})$$

where ε_s is dielectric constant.

5.3 Trap-assisted tunneling

Trap-assisted tunneling occurs when minority carriers tunnel from occupied trap states on quasi neutral side to the empty band states on the other side of the junction or through trap sites present in the depletion region of the junction. These trap centers are intermediate energy levels created by the presence of impurities in the material. The trap-assisted tunneling component of current density calculated on the basis of simple one dimensional model [10] can be written as

$$J_{TAT} = \frac{q^3 m_n^* E M^2 W N_T}{8\pi\hbar^3 (E_g - E_T)}\exp\left(-\frac{4\sqrt{2m_n^*(E_g - E_T)^3}}{3q\hbar E}\right) \quad (28\text{ a})$$

where E_g is the energy bandgap of the semiconductor, $\hbar = h/2\pi$, h being Plank's constant, E is the maximum electric field across the depletion region, E_T is energy (in eV) corresponding to trap centers, measured from top of the valence band, m_n^* is the effective mass of electron in the conduction band, N_T is the density of traps occupied by electrons. M is the matrix element associated with the trap potential [10].The resistance area product associated with trap assisted tunneling can be obtained as

$$\frac{1}{(RA)_{TAT}} = \frac{dJ_{TAT}}{dV}$$
$$= \frac{2q^3 m_n^* M^2 N_T}{8\pi\hbar^3 (E_g - E_T)}\exp\left(-\frac{B}{\sqrt{(V_{bi} - V)}}\right)\left(1 + \frac{B}{2\sqrt{(V_{bi} - V)}}\right) \quad (28\text{ b})$$

where

$$B = \frac{-4\sqrt{2m_n^*(E_g - E_T)^3}}{3q\hbar\sqrt{(2qN_A/\varepsilon_0\varepsilon_s)}}$$

5.4 Band-to band tunneling

At high reverse bias voltages, the cross over of energy bands takes place and electrons directly tunnel from the valence band from the p^+ side to the conduction band on the n side. This phenomenon is responsible for the flow of band to band tunneling current. The band-to-band tunneling component of current density can be obtained in the closed form as [9]

$$J_{BTB}=\frac{\sqrt{2m_n^*}q^3EV}{4\pi^2\hbar^2E_g^{1/2}}\exp\left(-\frac{4\sqrt{2m_n^*}E_g^{3/2}}{3qE\hbar}\right) \tag{29 a}$$

The corresponding resistance area product can be obtained by differentiating above equation with respect to V and taking the reciprocal. The band-to-band tunneling component of RA product can be obtained as

$$\frac{1}{(RA)_{BTB}}=\frac{q^3}{4\pi^2\hbar^2}\sqrt{\frac{2m_n^*}{E_g}}\exp\left(-\frac{4\sqrt{2m_n^*}E_g^{3/2}}{3q\hbar}\right)\left(E+\frac{V}{2(V_{bi}-V)}\left(E+\frac{4\sqrt{2m_n^*}E_g^{3/2}}{3q\hbar}\right)\right) \tag{29 b}$$

Considering the effect of all the two mechanisms discussed above, the net value of the resistance area product can be written as

$$\frac{1}{(RA)_{NET}}=\frac{1}{(RA)_{DIFF}}+\frac{1}{(RA)_{GR}}+\frac{1}{(RA)_{TAT}}+\frac{1}{(RA)_{BTB}} \tag{29 c}$$

5.5 Quantum efficiency

For computation of quantum efficiency (η) of N^+-$Hg_{0.69}$ $Cd_{0.31}Te$ /n^0 $Hg_{0.78}$ $Cd_{0.22}Te$ /p^+-$Hg_{0.78}$ $Cd_{0.22}Te$ p-i-n photodetector we have taken into account three major components. These components arise from the contribution of the three regions e.g., neutral p-region *(η_p)*, neutral n^0-region *(η_n)*, and the depletion region *(η_{dep})*. The optical generation rate of electron-hole pairs, as a function of distance x from the surface can be written as

$$G_n(x)=\frac{\alpha_n(\lambda)(1-R_{N^+})(1-R_{n^0})P_{opt}}{Ah\nu}\exp(-\alpha_n(\lambda)x) \tag{30}$$

$$G_p(x)=\frac{\alpha_p(\lambda)(1-R_{N^+})(1-R_{n^0})(1-R_{p^+})P_{opt}}{Ah\nu}\exp(-\alpha_p(\lambda)x) \tag{31}$$

where *$\alpha(\lambda)$* is the optical absorption coefficient of the material which is a function of wavelength λ, R_{N^+}, R_{n^0} and R_{p^+} are the Fresnel reflection coefficient at N^+, n^0 and p^+ interfaces, P_{opt} is the incident optical power, ν is the frequency of radiation and A is the device area. By solving continuity equations using appropriate boundary conditions at N^+-$Hg_{0.69}$ $Cd_{0.31}Te$ /n^0 $Hg_{0.78}$ $Cd_{0.22}Te$ hetero interface and at p^+ region and metal contact for holes and electrons respectively the quantum efficiency components can be obtained as

$$\eta_n=\frac{(1-R_{N^+})(1-R_{n^0})\,\alpha_n L_p}{\alpha_n^2L_p^2-1}\times\left[\left(\frac{\gamma_p\cosh\frac{(d-x_n)}{L_p}-\sinh\frac{(d-x_n)}{L_p}}{\cosh\frac{(d-x_n)}{L_p}-\gamma_p\sinh\frac{(d-x_n)}{L_p}}-\alpha_nL_p\right)\exp(-\alpha_n(d-x_n))-\left(\frac{\gamma_p\cosh\frac{(d-x_n)}{L_p}-\sinh\frac{(d-x_n)}{L_p}}{\cosh\frac{(d-x_n)}{L_p}-\gamma_p\sinh\frac{(d-x_n)}{L_p}}-1\right)\left(\frac{\alpha_nL_p-\gamma_p}{1-\gamma_p}\right)\exp\left(\frac{d-x_n}{L_p}\right)\right] \tag{32}$$

$$\eta_p=\frac{(1-R_{N^+})(1-R_{n^0})(1-R_{p^+})\,\alpha_p L_n}{\alpha_p^2L_n^2-1}\times\left[\left(\frac{\gamma_n\cosh\frac{(t_p-x_p)}{L_n}-\sinh\frac{(t_p-x_p)}{L_n}}{\cosh\frac{(t_p-x_p)}{L_n}-\gamma_n\sinh\frac{(t_p-x_p)}{L_n}}+\alpha_pL_n\right)\exp(-\alpha_p(d+x_p))-\left(\frac{\gamma_n\cosh\frac{(t_p-x_p)}{L_n}-\sinh\frac{(t_p-x_p)}{L_n}}{\cosh\frac{(t_p-x_p)}{L_n}-\gamma_n\sinh\frac{(t_p-x_p)}{L_n}}+1\right)\left(\frac{\alpha_pL_n+\gamma_n}{1+\gamma_n}\right)\exp(-\alpha_p(d+t_p))\exp\left(\frac{t_p-x_p}{L_n}\right)\right] \tag{33}$$

The contribution of the photo-generated carriers in the depletion region to the total quantum efficiency can be obtained as

$$\eta_{dep}=(1-R_{N^+})(1-R_{n^0})(1-R_{p^+})\{\exp(-\alpha_n(d-x_n))-\exp(-\alpha_p(d+x_p))\} \tag{34}$$

The net quantum efficiency can be written as

$$\eta=\eta_n+\eta_p+\eta_{dep} \tag{35}$$

Interface recombination velocity S_p at N^+-$Hg_{0.69}$ $Cd_{0.31}Te$ /n^0 $Hg_{0.78}$ $Cd_{0.22}Te$ interface has been modeled as [12-13]

$$S_p=\frac{n_{n^0}D_{pN^+}}{n_{N^+}L_{pN^+}}\frac{\left(\gamma_{pN^+}\cosh\left(\frac{t_{N^+}}{L_{pN^+}}\right)+\sinh\left(\frac{t_{N^+}}{L_{pN^+}}\right)\right)}{\left(\gamma_{pN^+}\sinh\left(\frac{t_{N^+}}{L_{pN^+}}\right)+\cosh\left(\frac{t_{N^+}}{L_{pN^+}}\right)\right)}\exp\left(\frac{-qV_{dN^+}}{kT}\right) \tag{36}$$

where n_{n^0} and n_{N^+} are refractive index of N^+ and n^0 regions respectively, V_{dN^+} is built in potential in the wide bandgap material at the isotype heterojunction, D_{pN^+}, L_{pN^+} and t_{N^+} are diffusion coefficient, diffusion length and thickness of N^+ region and γ_{pN^+} is ratio of surface to bulk recombination velocity in N^+ region.

5.6 Modeling of specific detectivity

The most important figure of merit of the photodetector for use in optical communication is the specific detectivity D^*, which depends on the wavelength of incident light λ, the quantum efficiency η and zero bias resistance area product, R_0A. As the dark current of the detector is contributed by three major components e.g., diffusion, generation-recombination and tunneling (which includes trap assisted tunneling (TAT) and band to band tunneling (BTB)), the detectivity of the photodetector under consideration should be estimated from the net value of R_0A product arising out of these mechanism. The specific detectivity of the photodetector which is a function of the applied voltage can be written as

$$D^* = \frac{q\eta\lambda}{hc}\sqrt{\frac{(R_0A)_{NET}}{4kT}} \tag{37}$$

5.7 Responsivity

The current responsivity ($\mathcal{R}$) of the photodetector is given as

$$\mathcal{R} = \frac{\eta q\lambda}{hc} \tag{38}$$

5.8 Noise equivalent power

The variation of noise equivalent power (NEP) with wavelength can be written as

$$NEP = \frac{A^{1/2}B^{1/2}}{D^*} \tag{39}$$

where A is the area of the detector and B is the bandwidth, here NEP is calculated at unity bandwidth (B=1Hz).

6. Results and discussion

Numerical computations have been carried out for N^+-$Hg_{0.69}Cd_{0.31}Te$ /n^0 $Hg_{0.78}Cd_{0.22}Te$ /p^+-$Hg_{0.78}Cd_{0.22}Te$ *p*-i-*n* photodetector at 77K. The light has been assumed to be incident from substrate side through N^+-$Hg_{0.69}Cd_{0.31}Te$. The incident photons with energy higher than the bandgap of $Hg_{0.78}Cd_{0.22}Te$ are absorbed in both the n^0 and p^+ regions. Various parameters used in the computations are listed in Table 1 and most of them were taken from reference [2].

Table 1.

Parameter	Values
x	0.22
E_g	$-0.302+1.93x-0.810x^2+0.832x^3+5.35\times10^{-4}(1-2x)\left(\frac{-1822+T^3}{255.2+T^2}\right)$ eV
Δ	1 eV
N_T	2.1×10^{19} m^{-3}
σ	4.7619×10^{-20} m^2
N_D	1.56×10^{19} m^{-3}
N_A	1×10^{23} m^{-3}
M^2	10^{-29} V^{2}m^3
S_p	10 m/s
S_n	10^3 m/s
χ	$4.23-0.813(E_g-0.083)$
N_c	3.793×10^{22} m^{-3}
N_v	5.1204×10^{24} m^{-3}
C_n	8.3×10^{-32} m^6/s
C_p	3.33×10^{-31} m^6/s
C_C^{OPT}	4.87×10^{-16} m^6/s

The different components of the dark current and *RA* product have been calculated using the theoretical model discussed in previous section. The variation of quantum efficiency, current responsivity, specific detectivity and Noise equivalent power (NEP) with wavelength at 77 K have been computed from the above mentioned model.

The proposed photodetector structure has also been simulated using device simulation software ATLAS™ from SILVACO® international. The device has been virtually fabricated using ATHENA tool of ATLAS™ software from SILVACO® international. The virtually fabricated structure is shown in Fig. 2. A program was developed separately for calculation of various characteristics of the photodetector using MATLAB platform by choosing appropriate material parameters.

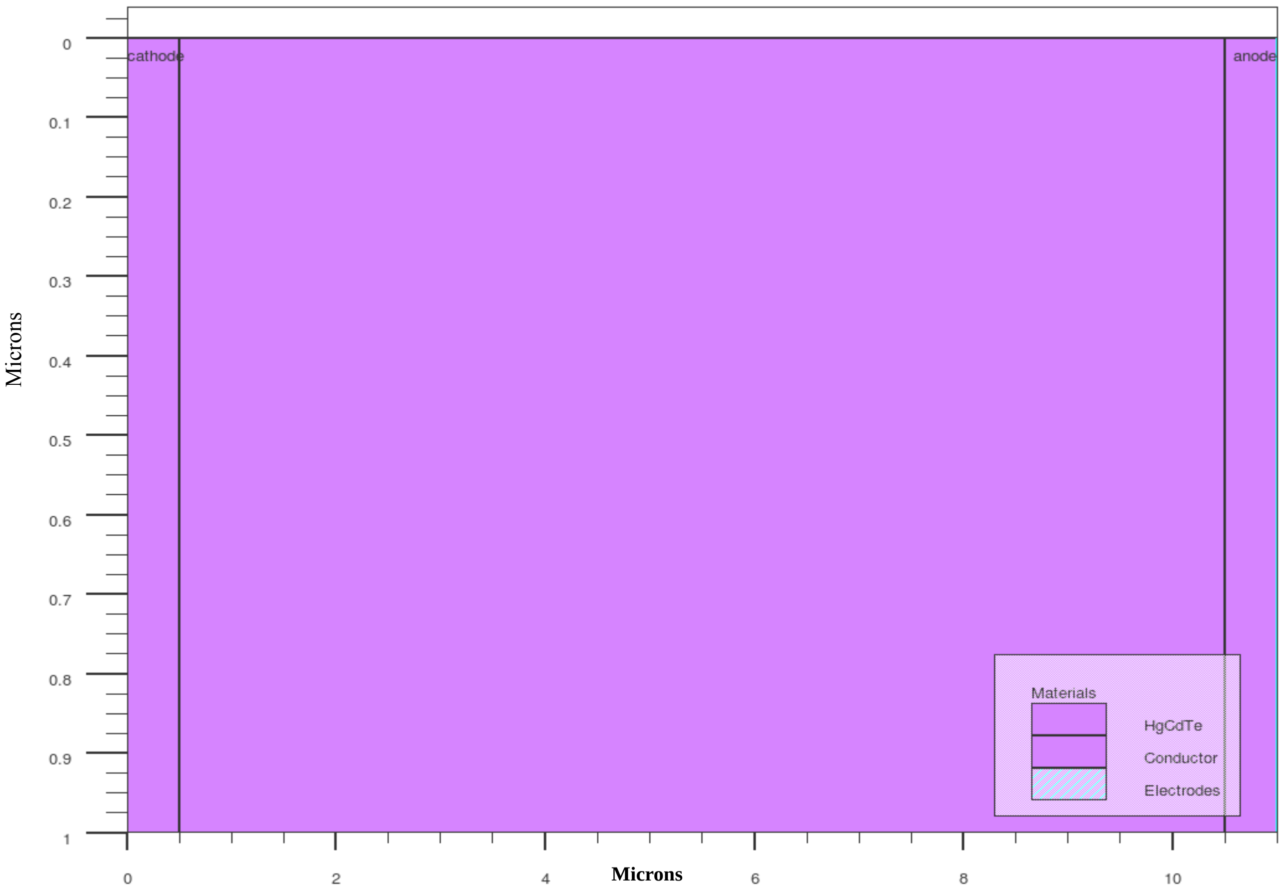

Fig. 2. Atlas simulated p-i-n photodiode structure.

The simulated results of p-i-n were obtained by developing program in DECKBUILD window interfaced with ATLAS for N^+-$Hg_{0.69}$ $Cd_{0.31}$Te /n^0 $Hg_{0.78}$ $Cd_{0.22}$Te /p^+-$Hg_{0.78}$ $Cd_{0.22}$Te *p*-i-*n* photodetector at 77K. Instead of the graded doping the numerical model includes a uniform doping profile. Once the physical structure of photodetector is built in ATLAS, the properties of the material used in device must be defined. A minimum set of material properties data includes, bandgap, dielectric constant, electron affinity, densities of conduction and valance band states, electron and hole mobility, optical recombination coefficient, and an optical file containing the wavelength dependent refractive index, n [14-15] and extinction coefficient *K* [14-15] for the used materials. The wavelength dependent values of extinction coefficient K is computed from the relation

$$K = \frac{\alpha\lambda}{4\pi} \tag{40}$$

The energy band diagram has been simulated from BLAZE, which is interfaced with ATLAS is a general purpose 2-D device simulator for III-V, II-VI materials, and devices with position dependent band structure (i.e., heterojunctions) [14]. BLAZE accounts for the effects of positionally dependent band structure by modifications to the charge transport equations. Equilibrium energy band diagram for electrons is shown in Fig. 3, has been simulated using BLAZE and its extended form is shown in Fig. 4 to show the notch and spike at the heterointerface for estimation of amount of discontinuity in the conduction band and valence band.

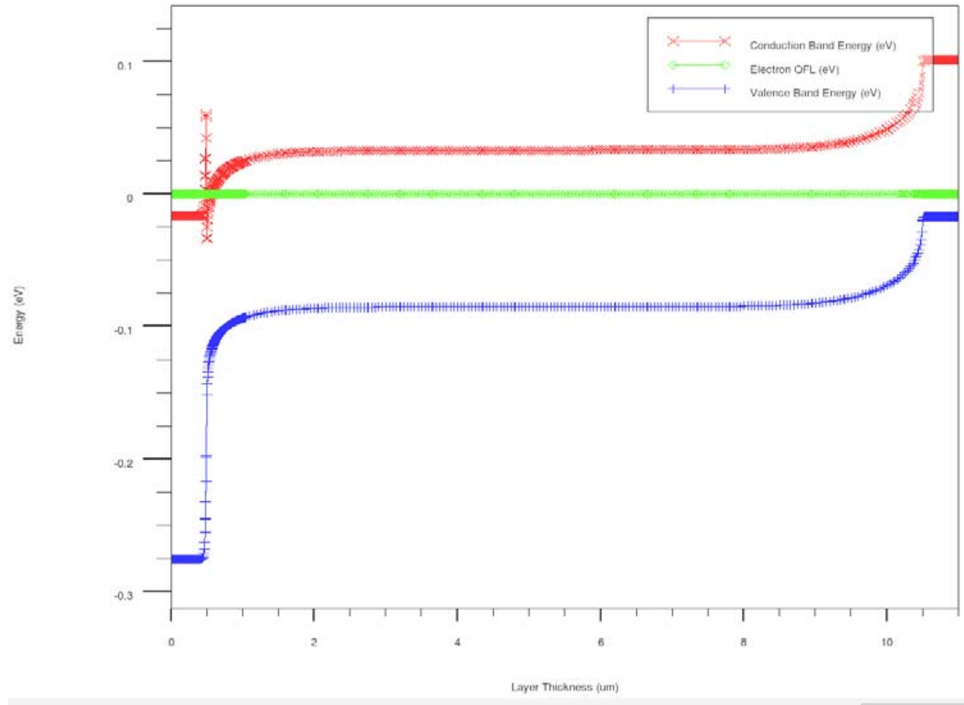

Fig. 3. Equilibrium energy band diagram.

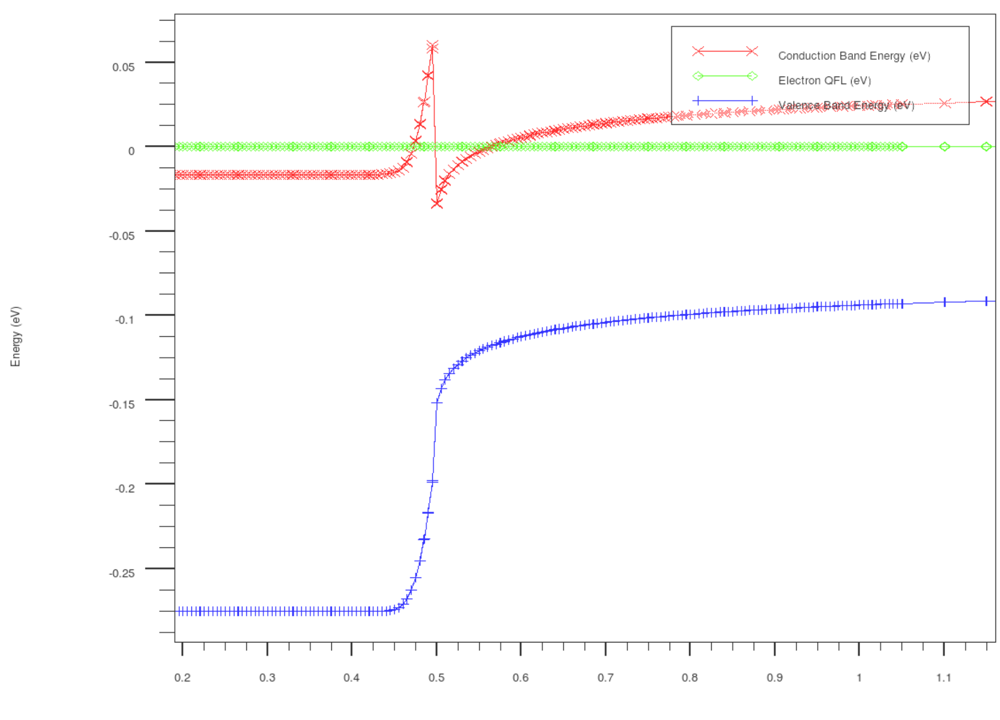

Fig. 4. Extended energy band diagram in equilibrium.

Fig. 5 shows electron energy band diagram of the device at three bias voltages (0V, 0.08V and 0.5V) in dark condition and extended form of the same is shown in Fig. 6 to show band discontinuity clearly.

Fig. 7, shows equilibrium Energy band diagram in dark and illuminated condition and Fig. 8 shows the same at V=0.5V.

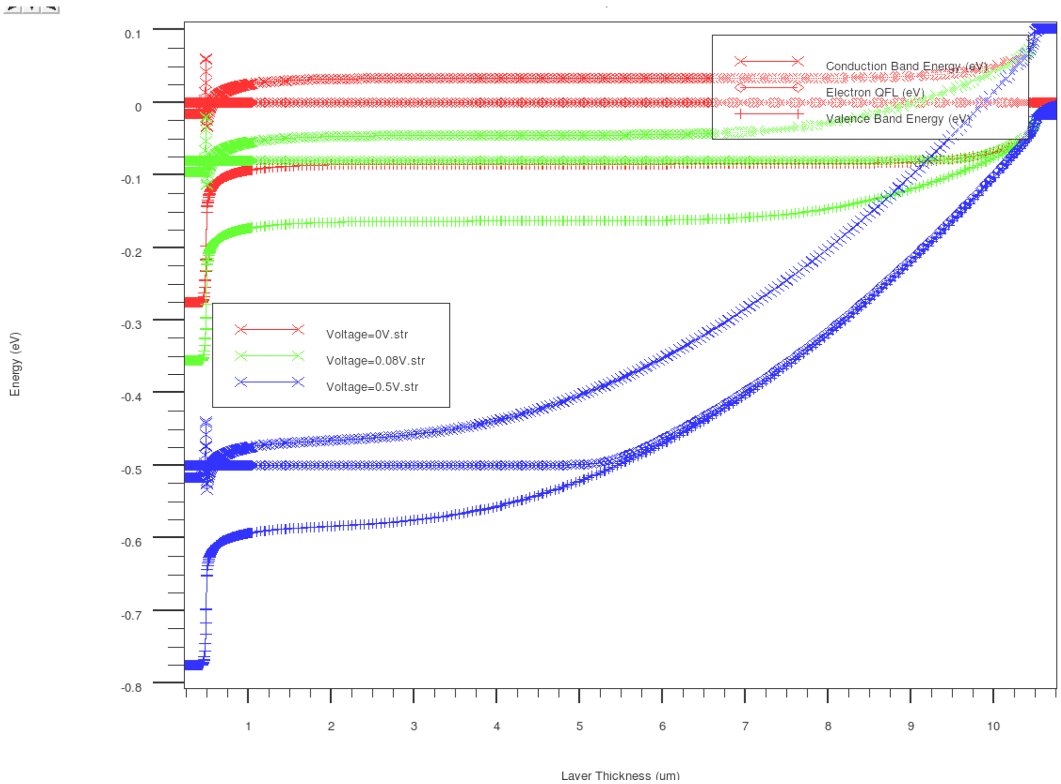

Fig. 5. Energy band diagram at different bias voltages in dark condition (at three bias voltages 0V, 0.08V and 0.5V).

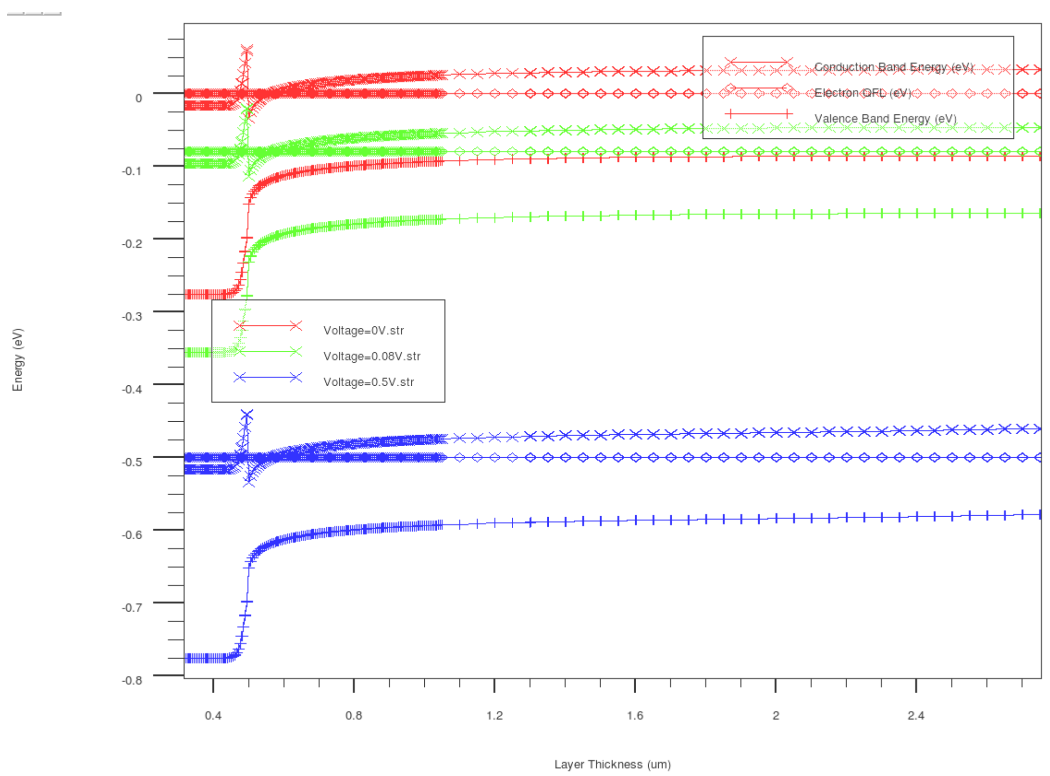

Fig. 6. Extended energy band diagram in dark condition at different bias voltages (at three bias voltages 0V, 0.08V and 0.5V).

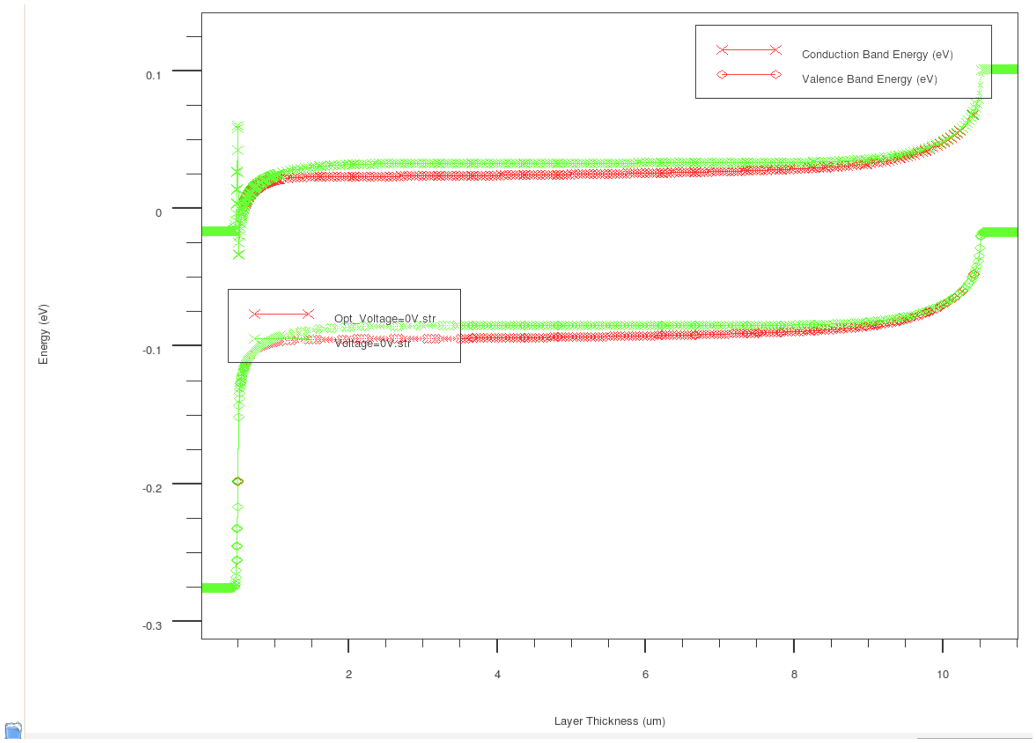

Fig. 7. Equilibrium energy band diagram in dark and illuminated conditions.

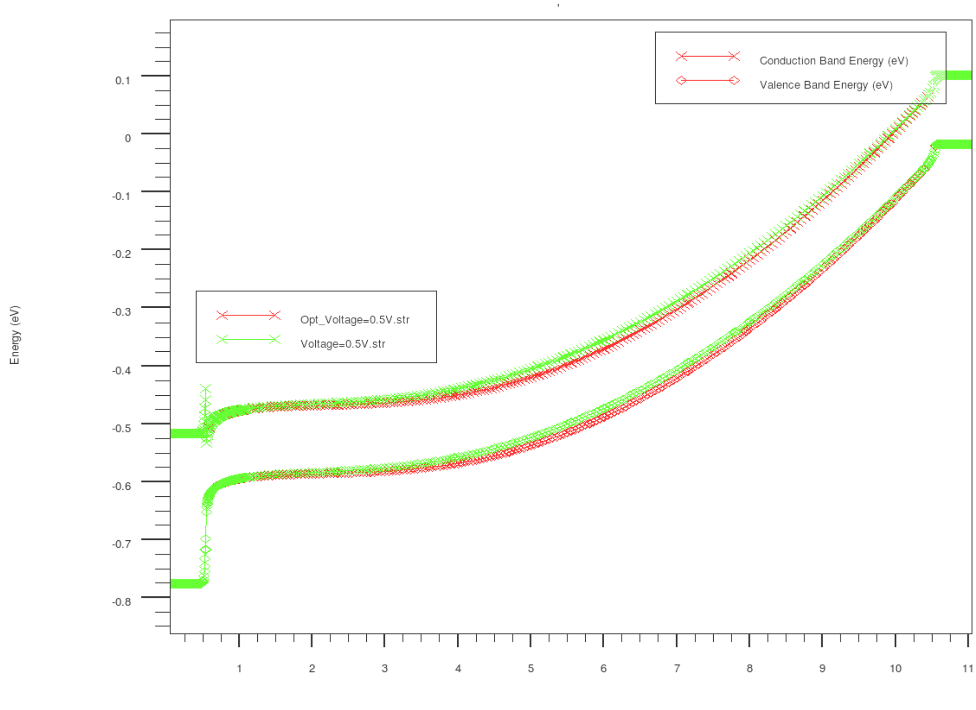

Fig. 8. Energy band diagram in dark and illuminated condition at V=0.5V.

Fig. 9 illustrates the energy band diagram at two different bias voltages (0V, 0.5V) in the illuminated condition. Equilibrium condition electric field profile of the photodetector is shown in Fig. 10. Fig. 11 illustrates electric field profile at two bias voltages (0V and 0.5V).

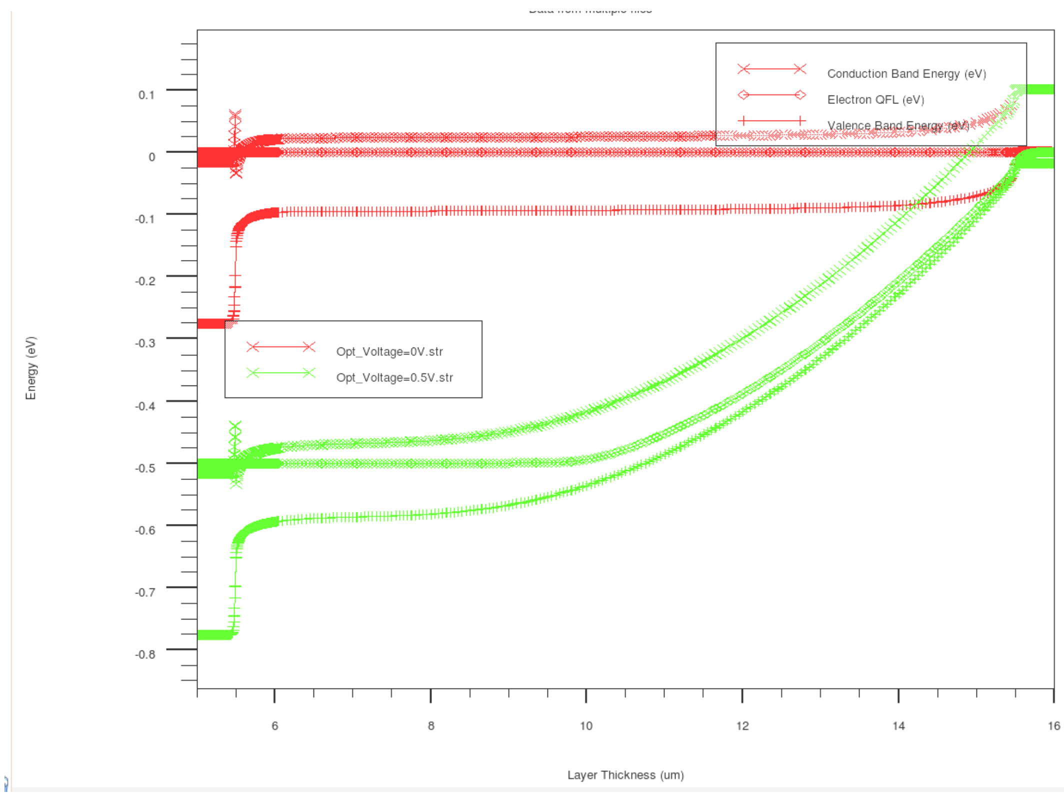

Fig. 9. Energy band diagram at different bias voltage in illuminated condition (0V, 0.5V).

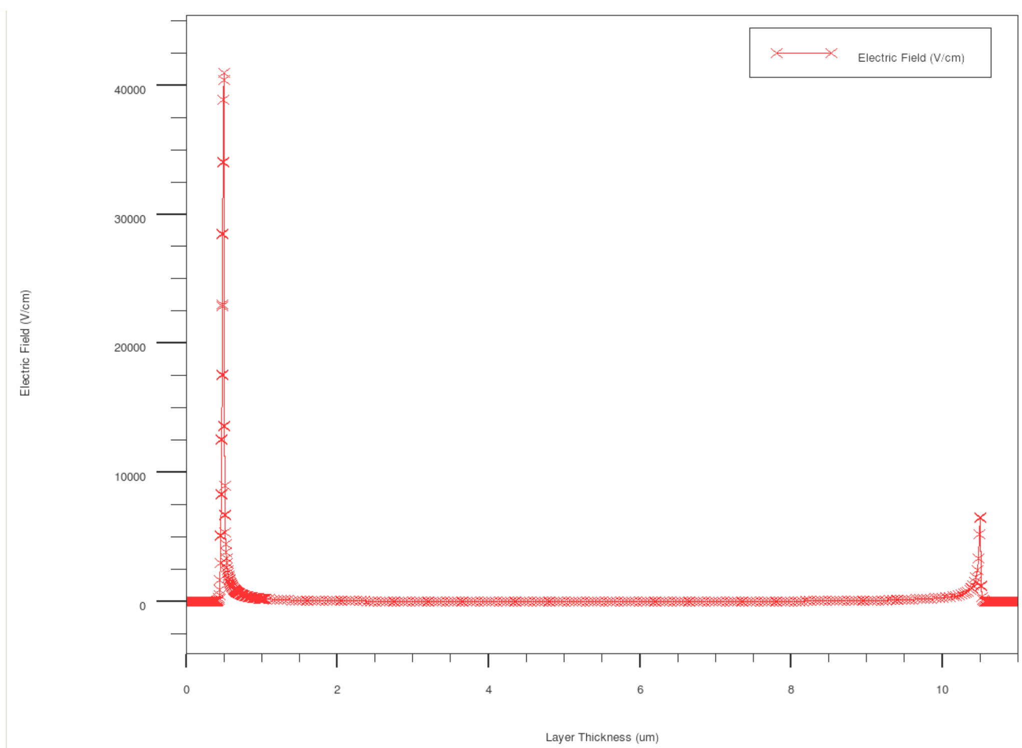

Fig. 10. Zero bias electric field profile of p-i-n photodiode.

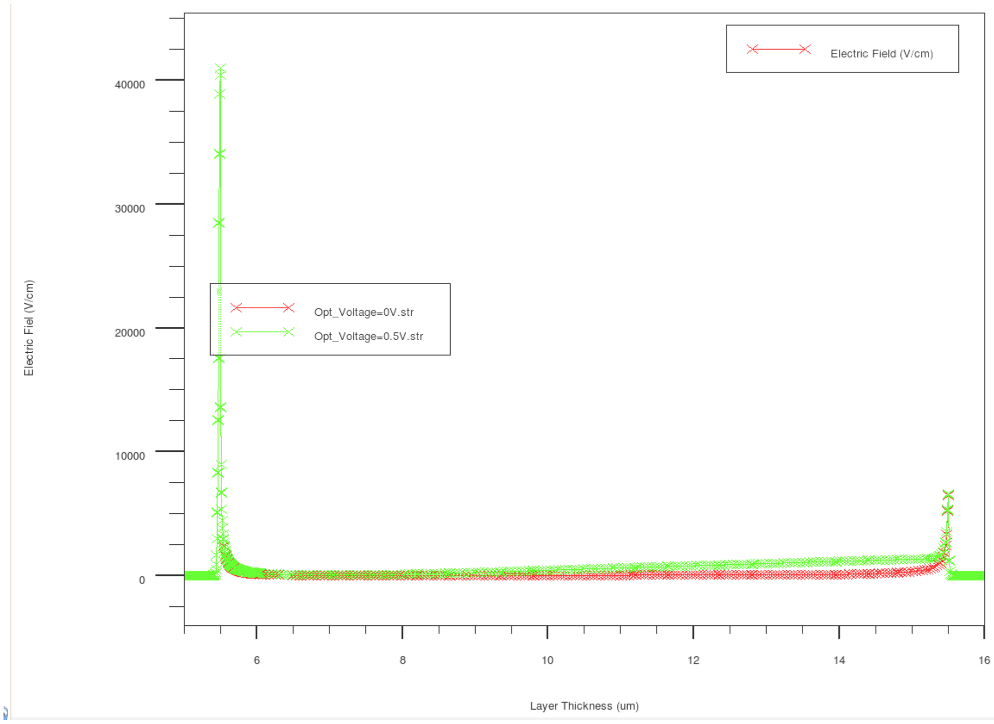

Fig. 11. Electric field profile in illuminated condition at (V=0V and V=0.5V).

Doping profile of the device is shown in Fig. 12 which shows, position dependent electron and hole concentration inside the device in different regions. Position dependent recombination rate at three different bias voltages is shown in Fig. 13. Variation of recombination rate with layer thickness of the device in illuminated condition at two bias voltages (0V and 0.5V) is shown in Fig. 14.

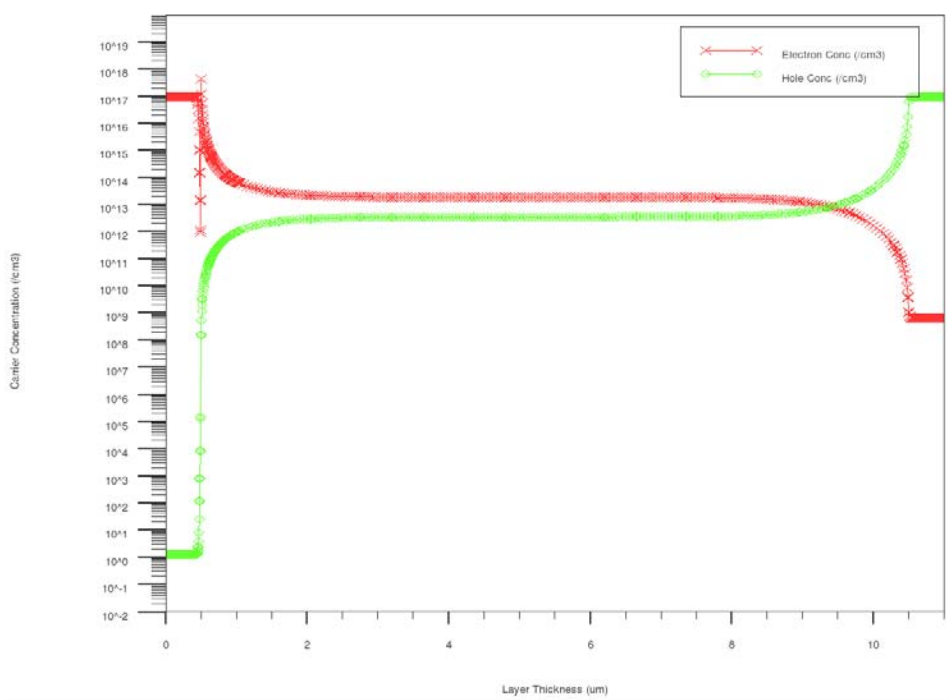

Fig. 12. Electron and hole concentration profile.

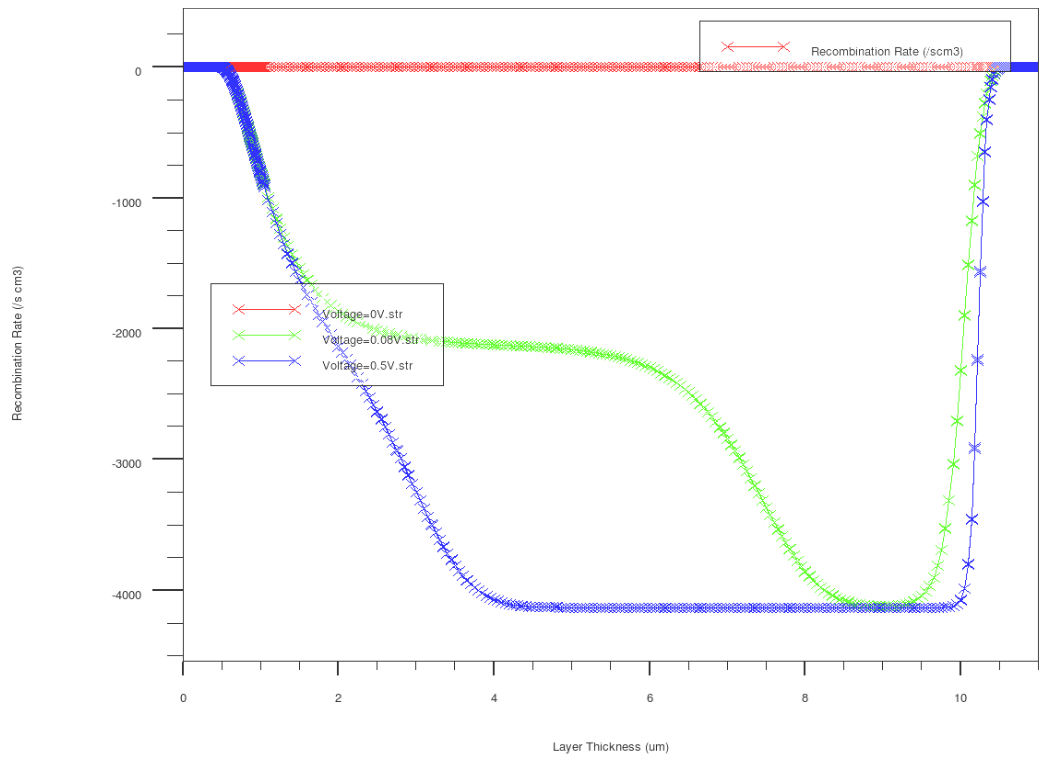

Fig. 13. Variation of recombination rate with layers thickness of the device in dark condition at three different bias voltages (0V, 0.08, 0.5V).

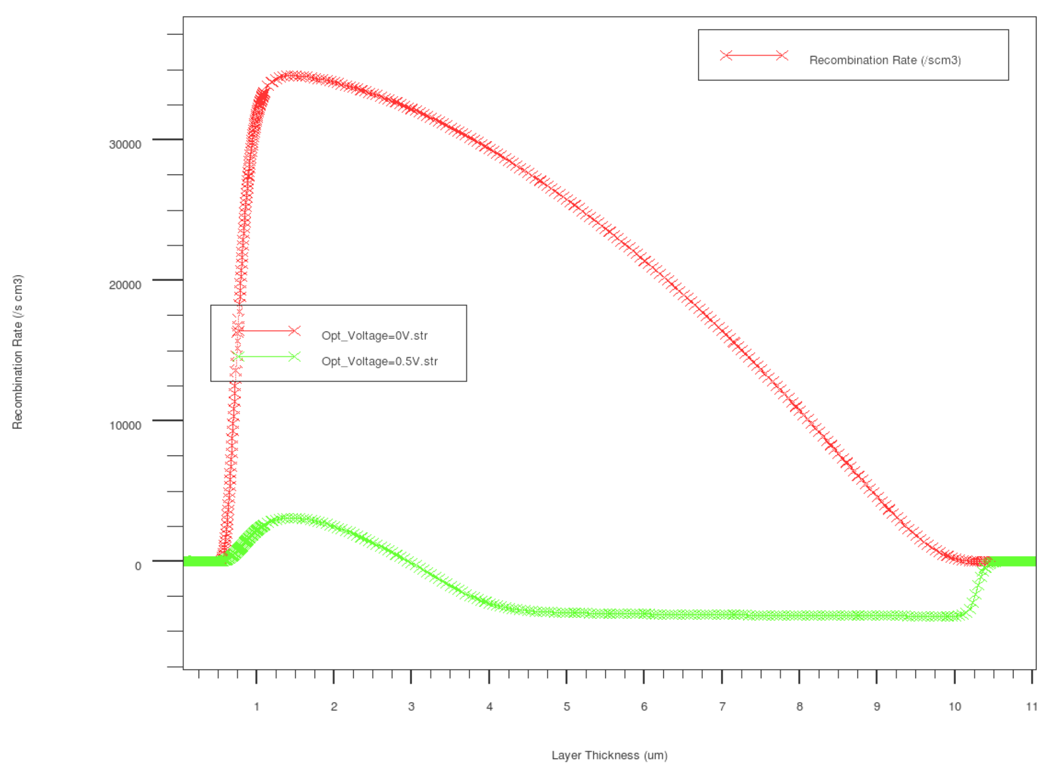

Fig. 14. Variation of recombination rate with layer thickness of the device in illuminated condition at two bias voltages (0V and 0.5V).

The optical characteristics of the device have been studied by using LUMINOUS tool of ATLAS device simulator. Of primary importance to the simulation of photodetector is the accurate modeling of electron hole pair generation. LUMINOUS, the optoelectronic simulation module in ATLAS, determines the photogeneration at each mesh point in an ATLAS structure by performing two simultaneous calculations. The refractive index n is used by LUMINOUS to perform an optical ray trace in the device. Difference in n values across the material boundaries determines the rate of light transmission and reflection. By following the path of light from the source to a mesh point, Luminous is able to determine the optical intensity at that point. Together, these simulations provide for wavelength dependent photogeneration throughout the photodetector [14-15]. The normalized spectral response of the photodetector is shown in Fig. 15.

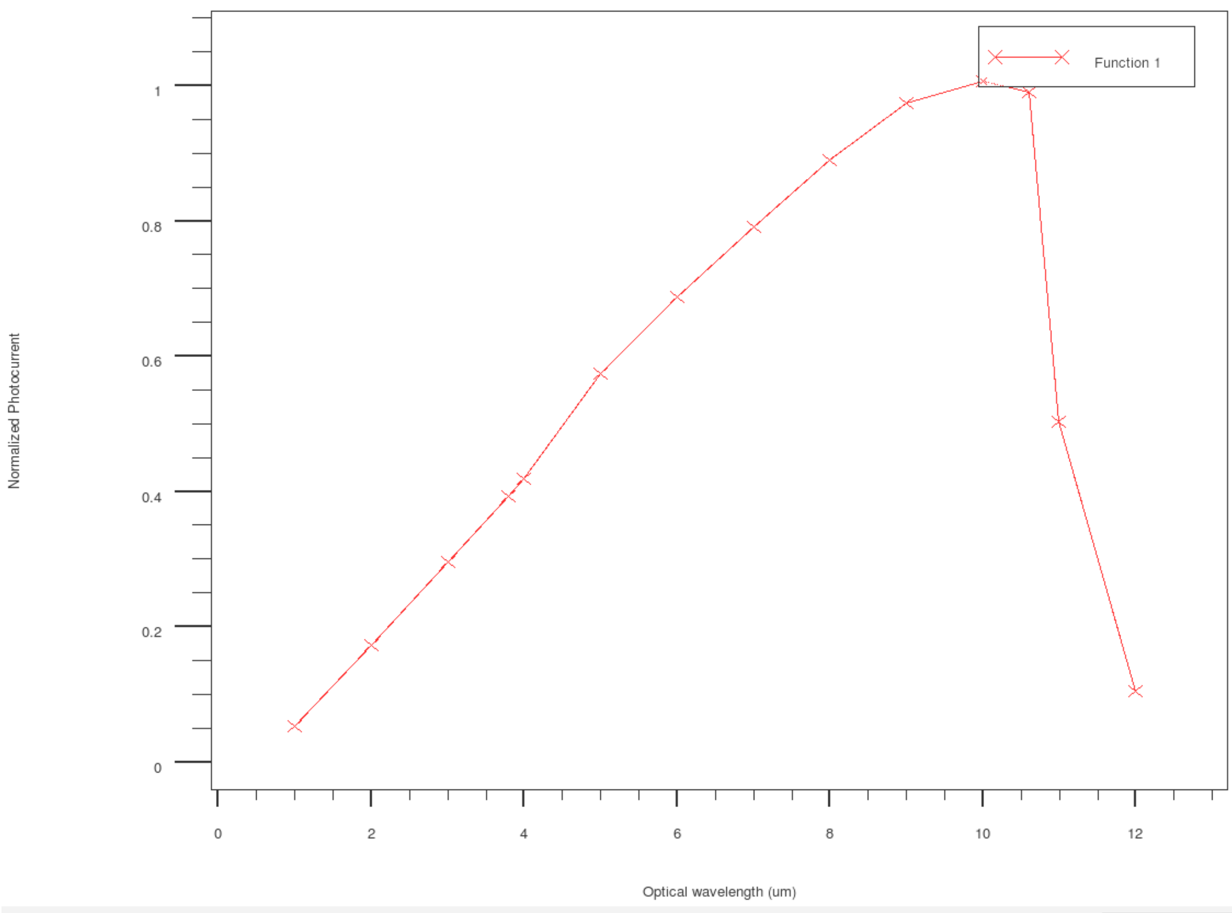

Fig. 15. Normalized spectral response of p-i-n photodiode at 0.5 V.

It is a plot between normalized terminal current in case of illumination with wavelength of operation. Normalized current increases with wavelength of operation and attains a maximum value at λ=10.6µm and there is a sharp fall beyond λ=10.6µm which is longer cut off wavelength for the proposed composition of the $Hg_{1-x}Cd_xTe$, which is absorbing layer in the proposed photodetector. The spectral response of the photodetector showing the variation of actual value of cathode current, source photocurrent and available photocurrent with wavelength is shown in Fig. 16. All the results discussed above have been obtained by ATLAS simulation.

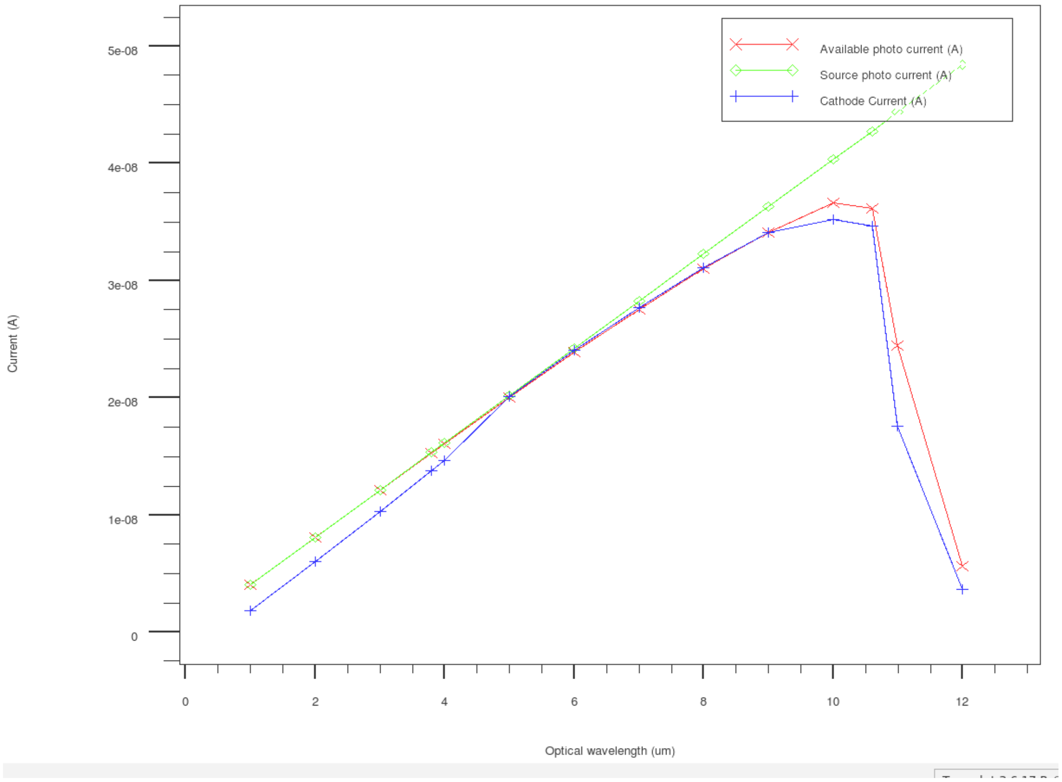

Fig. 16. Spectral response of the p-i-n photodiode at 0.5 V.

Fig. 17 shows variation of dark current with voltage as obtained from analytical model and ATLAS simulation. It is clear from this figure that there is a good agreement between dark current obtained from analytical model and that obtained from ATLAS simulation and device exhibits very low dark current of the order of 10^{-11} A.

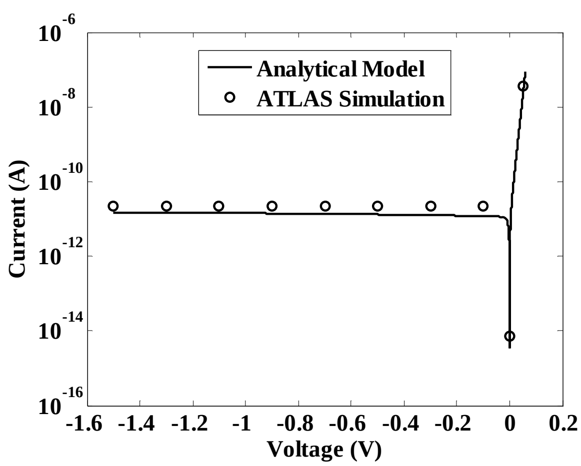

Fig. 17 Variation of dark current with voltage.

Variation of quantum efficiency of p-i-n photodetector with wavelength of operation as obtained from analytical model and ATLAS simulation at a bias voltage of 0.5V is shown in Fig. 18. From this figure it is clear that there is a good agreement in the quantum efficiency value estimated analytically and that computed on the basis of ATLAS simulation. The device exhibits very high quantum efficiency ~ 80% which attributes the high detectivity of the photodetector. This high quantum efficiency is obtained at the cost of bandwidth of the device because there is a trade off between quantum efficiency and 3 dB bandwidth. We can optimize the performance of the device by changing the doping concentration and dimensions of the device for high bandwidth performance but with lower quantum efficiency.

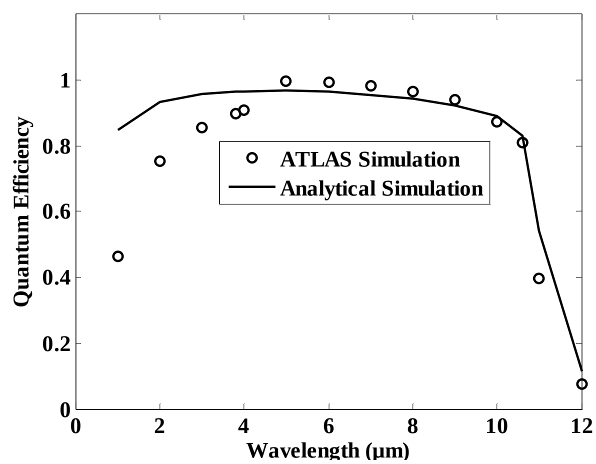

Fig. 18. Variation of quantum efficiency of p-i-n photodetector with wavelength (at V=0.5 V).

The variation of responsivity of the photodetector with wavelength of operation is shown in Fig. 19. From this figure we can see that there is a very good matching between responsivity obtained from analytical model and those obtained from ATLAS simulation. The device exhibits very high values of responsivity ~7A/W at wavelength 10.6µm and a bias voltage of 0.5V. Fig. 20 shows variation of specific detectivity with wavelength of operation, obtained by analytical model and also by ATLAS simulation which indicate that the order of the detectivity values as obtained by the two methods are very close. The device exhibits very high value of specific detectivity~3.44×10^{11} mHz$^{1/2}$W^{-1}at wavelength of operation 10.6µm and a bias voltage of 0.5V. Fig. 21 shows variation of noise equivalent power of the photodetector with wavelength of operation.

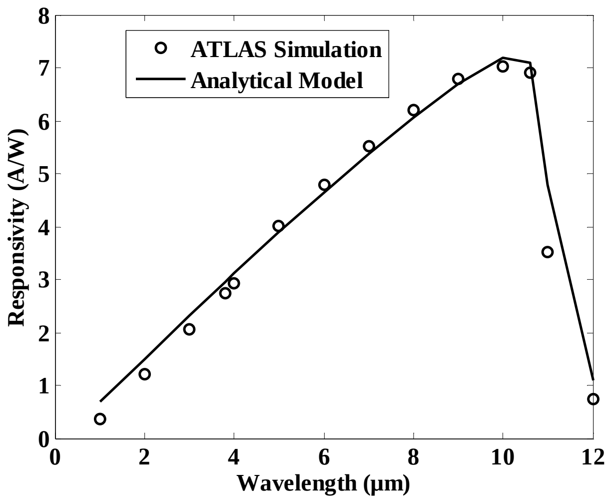

Fig. 19. Variation of responsivity with wavelength.

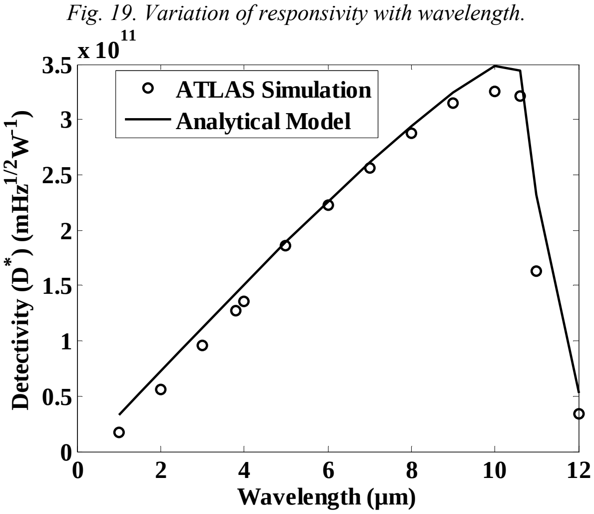

Fig. 20. Variation of detectivity of p-i-n photodiode with wavelength (at V=0.5 V).

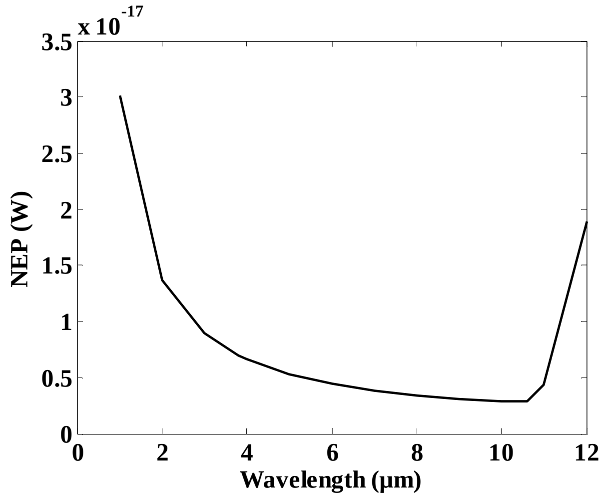

Fig. 21. Variation of noise equivalent power with wavelength.

We can see that the device exhibits a very low value of noise equivalent power (NEP) of the order of 3×10^{-18} W at the desired wavelength of operation 10.6 µm and NEP increases drastically beyond the upper cut off wavelength 10.6 µm of the detector and there is very small increment in NEP at wavelengths below 10.6 µm till 1 µm.

7. Conclusions

We proposed an N^+-$Hg_{0.69}Cd_{0.31}Te$ /n^0 $Hg_{0.78}Cd_{0.22}Te$ /p^+-$Hg_{0.78}Cd_{0.22}Te$ *p*-i-*n* photodetector for free space optical communication. The performance of the device has been examined by developing an analytical model for the dark current, quantum efficiency, responsivity and detectivity and results obtained from analytical model have been compared and contrasted by those obtained from ATLAS™ device simulation software from SILVACO® international. There is a very good agreement between results obtained by analytical model and those obtained from ATLAS simulation. The device exhibited a very low dark current of the order of 10^{-11} A, very high quantum efficiency~80%, responsivity~7A/W, detectivity~3.44×10^{11} mHz$^{1/2}$W^{-1}and noise equivalent power (NEP) ~ 3×10^{-18} W at wavelength of operation 10.6 µm and bias voltage of 0.5V. While the analytical model explores various physical mechanisms that shape the device characteristics, the simulation make use of advanced numerical technique to extract the performance of the p-i-n structure. A more rigorous noise analysis of the detector which accounts for various noise components arising out of the contribution of the photodetector and pre amplifier is currently under investigation.

References

[1] A. D. D. Dwivedi, P. Chakrabarti, Optical and Quantum Electronics **39**, 627 (2007).
[2] A. Rogalski, K, Adamiec, J. Rutokowski, SPIE Press, Bellingham, Washington, USA, 2000.
[3] P. Capper, Properties of Narrow Gap Cadmium-Based Compounds, EMIS data reviews series, No. 10, INSPEC, The institution of Electrical Engineers, London, 1995.
[4] M. H. Weiler, Semiconductors and Semimetals, Academic Press, New York, **16**, 119 (1981).
[5] J. Chu, Z. Mi, D. Tang, J. Appl. Phys. **71**, 3955 (1992).
[6] J. Chu, B. Li, K. Liu, D. Tang, J. Appl. Phys. **75**, 1234 (1994).
[7] J. Bardeen, F. J. Blatt, L. H. Hall, Photoconductivity Conference, Atlantic city 1954, 146, edited by R. Breackenridge, B. Russel, and E. Hahn, Wiley, New York, 1956.
[8] W. Shockley, W. T. Read, Phys. Rev. **87**, 835 (1952).
[9] P. Chakrabarti, A. Gawarikar, V. Mehta, D. Garg, Journal of Microwaves and Optoelectronics **5**(1), 1 (2006).
[10] V. Gopal, S. K. Singh, R. M. Mehra, Infrared Physics and Technology **43**, 317 (2002).
[11] P. Chakrabarti, A. Krier, A. F. Morgan, IEEE Trans. On Electron Devices **50**, 2049 (2003).
[12] Tian Yuan, Chua Soo Jin, Yixin Jin, Microelectronics Journal **34**, 305 (2003).
[13] Tian Yuan, Soo-Jin Chua, Yixin Jin, Infrared Physics and Technology **45**, 181 (2004).
[14] ATLAS User's manual Version 5.10.0.R, SILVACO International, Santa Clara, CA 95054, 2005.
[15] A. D. D. Dwivedi, P. Chakrabarti, International Conference on Recent Advances in Microwave Theory and Applications (MICROWAVE-2008), 412, 21-24, November 2008.

*Corresponding author: pchakrabarti.ece@itbhu.ac.in